Microfluidics and Nanofluidics (2018) 22:101
https://doi.org/10.1007/s10404-018-2122-9

RESEARCH PAPER

Experimental study of drying effects during supercritical CO_2 displacement in a pore network

Ying Wang[1] · **Ning Wei**[2] · **Changyong Zhang**[3] · **Thomas W. Wietsma**[3] · **Alain Bonneville**[3] · **Xiaochun Li**[2] · **Min Li**[1] · **Zheming Wang**[3]

Received: 22 February 2018 / Accepted: 21 August 2018 / Published online: 25 August 2018

Abstract

Underground storage in geological aquifers is one of the most important options for large-scale mitigation of CO_2. During the supercritical CO_2 ($scCO_2$) injection process, water dissolved in $scCO_2$ may have significant impact on the displacement process. In this study, a series of wet $scCO_2$ ($WscCO_2$, 100% water saturation) and dry $scCO_2$ ($DscCO_2$, 0% water saturation) displacement experiments were conducted in micromodels for a large range of flow rates. The displacement was visualized using fluorescence microscopy. Results showed that $DscCO_2$ saturations were up to 3.3 times larger than $WscCO_2$ saturations when the capillary fingering dominated the displacement. The specific interfacial areas and mobile fractions for the $DscCO_2$ displacements were also much larger than those for $WscCO_2$. The capillary forces combined with drying effects are identified as the leading causes for the considerably higher $DscCO_2$ sweep efficiency. Results from this study showed the important impact of mutual solubility of $scCO_2$ and water on the displacement process and saturation of $scCO_2$ (S_{scCO2}), suggesting that the conventional model describing the relationship between capillary pressure and S_{scCO2} needs to be modified for the effect of the mutual dissolution of multiple phases to more adequately describe the $scCO_2$ displacement process in saline aquifer formation.

Keywords Drying effects · CCS · $scCO_2$–water displacement · Mutual dissolution · Micromodel

1 Introduction

CO_2 storage in deep saline aquifer formation is considered an important option to mitigate CO_2 emission to the atmosphere (Metz et al. 2005). After its capture from a concentrated source (e.g., coal power plant), CO_2 is injected into deep permeable geological formations causing formation fluids (e.g., brine) to be displaced. Among various factors that may limit the storage efficiency, hydraulic properties of the porous media and the interfacial properties of CO_2 and formation fluids are expected to play important roles in affecting fluid flow, plume development and saturation levels (Zhang et al. 2011a; Wang et al. 2013a).

The displacement process of brine by $scCO_2$ is commonly treated as an immiscible system considering the low solubility between different phases, thus asserting a major effect on each other's displacement. However, the mutual solubility between $scCO_2$ and brine (Spycher et al. 2003; Lu et al. 2009) can be high, particularly at higher temperatures in deeper aquifers, which may affect the displacement process and flow properties at the pore scale: (i) the mutual

---

Electronic supplementary material The online version of this article (https://doi.org/10.1007/s10404-018-2122-9) contains supplementary material, which is available to authorized users.

✉ Ying Wang
yingwang2017@icloud.com

✉ Ning Wei
nwei@whrsm.ac.cn

[1] State Key Laboratory of Oil and Gas Reservoir Geology and Exploitation, Southwest Petroleum University, Chengdu 610500, China

[2] State Key Laboratory for Geomechanics and Geotechnical Engineering, Institute of Rock and Soil Mechanics, Chinese Academy of Sciences, Wuhan 430071, China

[3] Pacific Northwest National Laboratory, 902 Battelle Boulevard, MSIN K8-96, P. O. Box 999, Richland, WA 99352, USA

dissolution affects the physical properties, such as interfacial tension, viscosity, and density. The variation of interfacial tension between the two phases alters the capillary forces, and thus the fingering patterns; (ii) $scCO_2$ extracts water in the pore spaces and increases the salinity of brine, and even causes salt precipitation and porosity/permeability reduction, which is commonly called dry-out effect (Pruess 2009; Pruess and Müller 2009).

Recently, a growing body of modeling and experimental research across multiple spatial scales has been conducted to investigate the effects of dissolved CO_2 in aqueous formations, including mineral precipitation/dissolution as well as rock porosity and permeability modification (Nordbotten et al. 2005; Xu et al. 2005; Lu et al. 2009; Pruess 2009; Pruess and Müller 2009; Zhou et al. 2010; Lopez et al. 2011; Sohrabi et al. 2011; McCaughan et al. 2013). For instance, Pruess et al. investigated the effects of CO_2 dry-out resulting in salt precipitation, potentially interfering with injection operations by simulation code TOUGH2 (Xu et al. 2005; Pruess and Müller 2009). According to their study, even the water solubility in $scCO_2$ is only a fraction of a percent, and continuous injection of $DscCO_2$ into saline aquifers may eventually lead to complete formation dry out which will cause dissolved solids to participate. Bachu and Bennion found that capillary pressure, IFT (interfacial tension), and relative permeability depend on pressure, temperature and water salinity, as well as the pore-size distribution of the sedimentary rock in $scCO_2$–brine systems in deep saline aquifer formations (Bennion and Bachu 2005, 2006a, b, c, 2007a, b, 2008; Stefan Bachu and Brant; Bennion 2008; Bachu and Brant Bennion 2009). However, research related to the following issues is limited: (i) potential advantages of $scCO_2$ dry-out effect which may enhance the $scCO_2$ sweep efficiency (i.e., the ratio of areas of displacement and reservoir). (ii) The effect of the dissolved water in $scCO_2$ which may alter the $scCO_2$ sweep efficiency. So far, the dissolved water in $scCO_2$ is ignored in most works because of the relatively low solubility of water in $scCO_2$, and the fact that below 100 °C the viscosity of water-containing $scCO_2$ is close to that of pure $scCO_2$. However, now it is known that the dissolved water in $scCO_2$ drastically enhances the activities of $scCO_2$ with rock minerals (e.g., $CaCO_3$) (Loring et al. 2010), indicating that the dissolved water plays a significant role in $scCO_2$–brine displacement process (Wang et al. 2013b).

In the two-phase immiscible displacement process of water displaced by CO_2, the CO_2 is a non-wetting phase and the water is a wetting phase. Over the last three decades, fundamental understanding of the mechanisms that control immiscible two-phase flow under ambient pressure and temperature conditions has been gained through abundant pore-scale experiments using microfabricated physical models of porous media (i.e., micromodels) and a variety of pore network modeling approaches (Lenormand et al. 1988; Ferer et al. 2004; Nordbotten et al. 2005; Cottin et al. 2010; Zhou et al. 2010; Hatiboglu and Babadagli 2010; Lengler et al. 2010; Zhang et al. 2011a, b; Zhao et al. 2011; Wang et al. 2013a; Mohammadi et al. 2013; Kazemifar et al. 2016; Roman et al. 2016; Takeshi et al. 2016). Displacement of a wetting phase by a non-wetting fluid in a 2D pore network, commonly referred to as main drainage, is often described by two dimensionless numbers, the capillary number *Ca* and the viscosity ratio *M*. Here,

$$\mathrm{Ca} = (\mu_\mathrm{n} \times u_\mathrm{n})/(\sigma_\mathrm{nw} \times \cos\ \theta) \text{ and } M = \mu_\mathrm{n}/\mu_\mathrm{w}, \tag{1}$$

where μ_n and u_n are the viscosity and velocity of the invading non-wetting fluid, respectively, σ_nw is the interfacial tension, θ is the contact angle, and μ_w is the viscosity of the initially residing wetting fluid. Depending on Ca and M, different mechanisms, including capillary fingering, crossover, viscous fingering and stable displacement, have been shown to control immiscible displacement at pore scale (Wang et al. 2013a).

For immiscible fluid displacement with low viscosity ratios (i.e., $\log M < 0$) which is the case of the $scCO_2$–water systems, the three mechanisms of capillary fingering, crossover and viscous fingering control the fluid flow, respectively, along with increase in Ca number (Wang et al. 2013a). In a previous study (Ferer et al. 2004), it was found that the $scCO_2$ saturation (S_{scCO2}) was very high during capillary fingering dominant period, confirming observations under ambient conditions by Ferer (Lenormand et al. 1988) and (Mahadevan et al. 2007; Pruess and Müller 2009). In these studies, the mutual solublities and the corresponding disturbances to each other were not considered because of the nearly zero mutual solubility between the nonaqueous phase and aqueous phase during the displacement process. However, with the drying effects of CO_2, at the interfacial area of CO_2 and brine, the $DscCO_2$ will dissolve into the aqueous phase and water will dissolve into CO_2, and the displacement system between $DscCO_2$ and water cannot merely be considered as an immiscible displacement process (Spycher et al. 2003; Wang et al. 2013b). So far, the impacts of the drying effects from $DscCO_2$ and the influence of the dissolved water in $WscCO_2$– on the $scCO_2$–water displacement process are unclear.

In this study, we expand our work to further interrogate the capillary forces combined with drying effects relevant to $DscCO_2$–water displacement at the pore scale under reservoir conditions. Specifically, we focus on $DscCO_2$– and $WscCO_2$–water displacements, respectively, in two near homogeneous pore networks micromodels with well-defined surface property and pore geometry and different inlet and outlet designs over a broad range of injection rates ($\log\mathrm{Ca} = -7.64 \sim -4.76$) under high pressure (9 MPa) and temperature of $scCO_2$ (> 31 °C). The displacement process was observed in real time using fluorescence microscopy and

S_{scCO2} was quantitatively evaluated from fluorescent images. Results obtained from experiments about the saturation of $DscCO_2$ were compared with that of $WscCO_2$ at the same Ca, to analyze the drying effects from $DscCO_2$ and the influence of the dissolved water in $WscCO_2$ on S_{scCO2}.

2 Experimental methods

2.1 Fluids

Distilled and deionized water (DDI) and supercritical fluid chromatography (SFC)-grade $scCO_2$ were used as the wetting and non-wetting phases, respectively. The non-wetting $scCO_2$ was classified as either $DscCO_2$ or $WscCO_2$, with a dissolved water content of 0 and 100%, respectively. Based on our previous work, the water saturation concentration in $scCO_2$ at 40 °C and 35 °C are 0.32 and 0.49 mol%, respectively (Choi et al. 1998; Zhang et al. 2011a; Wang et al. 2013a). $WscCO_2$ was made by injecting 1 ± 0.1 mL water into Pump A [Figure S1(c), in Supporting Information (SI)] that was filled with 28.9 ± 1.5 mL $scCO_2$. The presence of excess water ensures saturation level water concentration in $scCO_2$ at 35 or 40 °C over 12 h. Table 1 summarizes the properties of the wetting and non-wetting fluids. Since the density, viscosity and interfacial tension (IFT) of $WscCO_2$

Table 1 Summary of experimental conditions, fluid properties, volumetric flow rates and the corresponding Darcy velocity and capillary number

Fluid properties	
Viscosity $scCO_2$ 40 °C/35 °C (mPa s)[e]	0.035/0.051[a]
Density $scCO_2$ 40 °C/35 °C (g/cm^3)[e]	0.486/0.662[a]
Viscosity water 40 °C/35 °C (mPa s)	0.65/0.72
Density water 40 °C/35 °C (g/cm^3)	0.996/0.998
log$M$ 40 °C/35 °C [−][e]	− 1.1/− 1.1
Interfacial tension 40 °C/35 °C [mN/m][e]	26.2/25.2[b]
$scCO_2$/water contact angle (°)[e]	14.7 ± 0.3[c]
$scCO_2$ entry pressure 40 °C/35 °C (Pa)[e]	3.79/3.65[d]
Experimental conditions	
Pressure (MPa/psi)	9/1305
Temperature (°C)	40 ± 1/35 ± 1

Flow rate Q (μL/h)	Darcy velocity v (m/d)	logCa [−] 40 °C/35 °C
Volumetric flowrates		
10	0.57	− 7.64/− 7.46
100	5.67	− 6.64/− 6.46
1000	56.67	− 5.64/− 5.46
5000	283.35	− 4.94/− 4.76

Series no.	Fluids	Micromodel	logCa [−]	Temperature (°C)
Displacement experiments				
Set I	$DscCO_2$–water $WscCO_2$–water	M-1	− 7.64, − 6.64, − 5.64, − 4.94	40
Set II	$DscCO_2$–water $WscCO_2$–water	M-2	− 7.64, − 6.64, − 5.64, − 4.9	40
Set III	$DscCO_2$–water $WscCO_2$–water	M-2	− 7.46, − 6.46, − 5.46, − 4.76	35

[a] Nordbotten et al. (2005)

[b] Bachu and Bennion (2009)

[c] Measured in this study. An image of the $DscCO_2$–water contact angle with micromodel surface in the outlet channel is included in the Supporting Information (Figure S6). The $WscCO_2$–water contact angle was measured to be approximately the same as that of $DscCO_2$–water

[d] Computed using equation $P_c = (1/r_1 + 1/r_2)\cos\theta$

[e] In this study, the fluid properties of $DscCO_2$ were obtained from the above publications. Since the fluid properties (e.g., density and viscosity) of $WscCO_2$ have not been published,they were estimated by empirical calculation of gas mixtures (Equation S1 in Supporting Information). The interfacial tension of $WscCO_2$–water was also assumed to be the same as that of $DscCO_2$–water

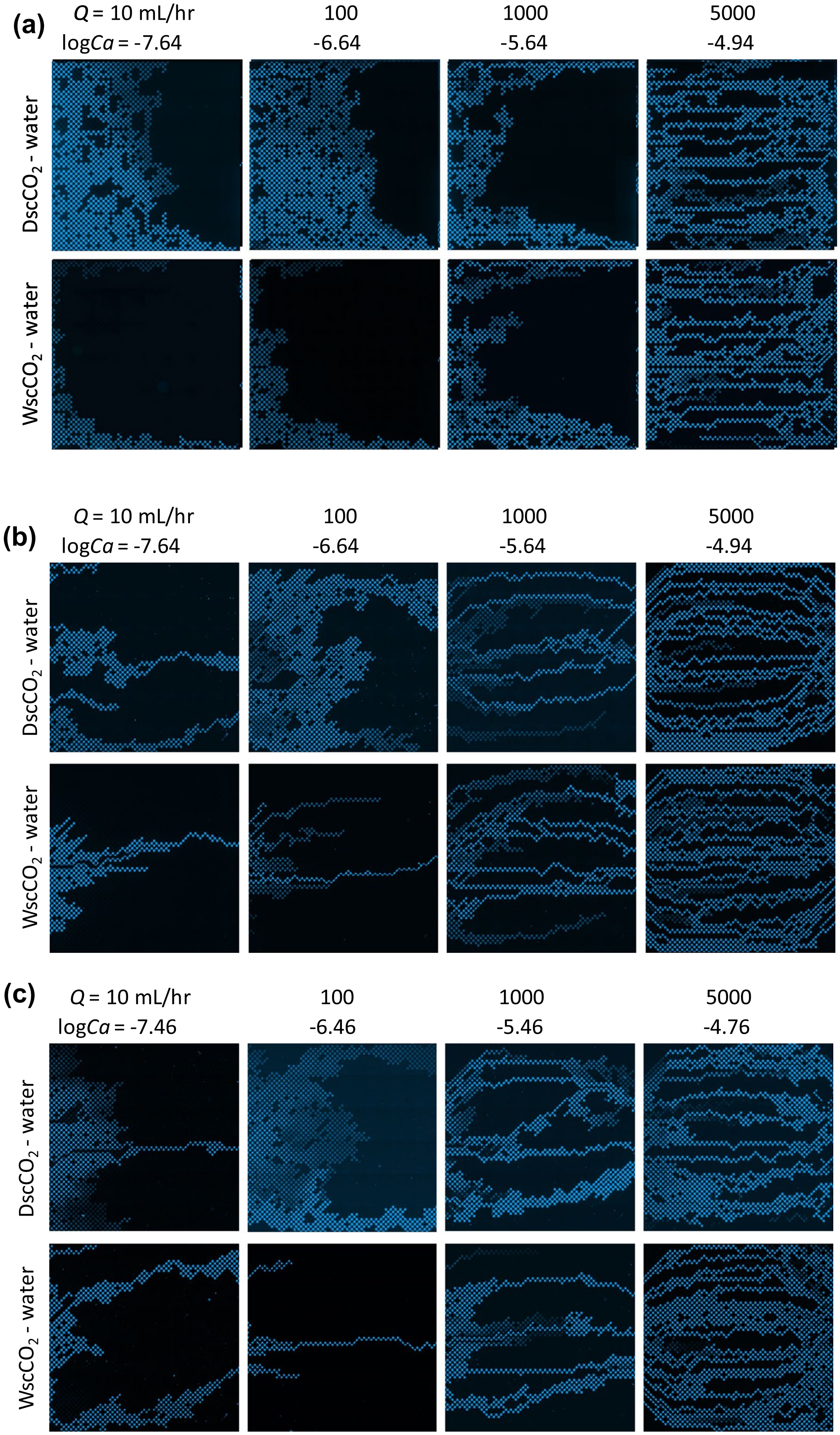
(a)
Q = 10 mL/hr
100
1000
5000
logCa = -7.64
-6.64
-5.64
-4.94
DscCO2 - water
WscCO2 - water
(b)
Q = 10 mL/hr
100
1000
5000
logCa = -7.64
-6.64
-5.64
-4.94
DscCO2 - water
WscCO2 - water
(c)
Q = 10 mL/hr
100
1000
5000
logCa = -7.46
-6.46
-5.46
-4.76
DscCO2 - water
WscCO2 - water

◂**Fig. 1** $scCO_2$ (blue) distribution at various injection rates (logCa) for the $DscCO_2$– and $WscCO_2$–water experiments in: **a** M-1 micromodel at 40 °C. **b** M-2 micromodel at 40 °C. **c** M-2 micromodel at 35 °C. The $scCO_2$ flow is from left to right. The numbers indicate the logCa and the coresponding injection rate *Q*

have not been published and experimental measurement of them in our laboratory is not feasible, in this study the viscosity and density were estimated by empirical calculation of the gas mixtures (Equation S1 in SI). The results indicated that the density and viscosity of $WscCO_2$ were almost the same as those of $DscCO_2$. The contact angle between $DscCO_2$ and water and that between $WscCO_2$ and water was also determined to be approximately the same in this study (Figure S6). Similarly, the IFT between $WscCO_2$ and water was considered to be the same as that between $DscCO_2$ and water. From the above, those properties required to calculate the Ca of $WscCO_2$ are almost the same as those of $DscCO_2$.

A fluorescent dye, Coumarin 153 (99.99%; Alfa Aesar, Ward Hill, MA), was added to $scCO_2$ to distinguish $scCO_2$ from water using fluorescent microscopy. Coumarin 153 absorbs in the near UV and emits in the broad spectral range from 450 nm to over 600 nm. Details of Coumarin 153 characteristics can be found in the literature (Chomsurin 2003; Willingham et al. 2008; Zhang et al. 2011a, b; Wang et al. 2013a). All chemicals are ACS-reagent-grade (Sigma–Aldrich). In this study, a stock solution of Coumarin 153 was prepared in methanol at a concentration of 10 mM, and then 1 mL stock solution was added to the cylinder of Pump A (shown in Figure S1(c) in SI). The methanol can be evaporated and the Coumarin 153 can be fully mixed by purging the cylinder with $scCO_2$ for over 10 h.

2.2 Micromodels

The micromodels were fabricated using microfabrication procedures described in previous studies (Zhang et al. 2011a; Wang et al. 2013a). Two types of micromodels, M-1 and M-2 (Figure S1(a) and S1(b), in SI), were used as the pore networks in this work. The overall pore geometry of both was the same, except for the inlet and outlet boundaries in model M-2, for which the inlet and outlet channels were filled with grains to simulate the effects of different boundary conditions on the distribution of $scCO_2$ plume. Both micromodels M-1 and M-2 have similar homogeneous network of cylindrical grains (200 µm diameter) and pore spaces (120 µm pore bodies, 26.7 µm pore throats), and average pore depth (35 ± 1 µm).

2.3 $scCO_2$–water displacement

The high-pressure micromodel experimental system (Figure S1(c)) has been described in detail previously (Lenormand et al. 1988; Ferer et al. 2004; Zhang et al. 2011a, b; Wang et al. 2013a). A total of four different volumetric injection rates ranging from 10 to 5000 uL/h were applied (Table 1). The imposed flow rates correspond to a range in the converted Darcy velocity from 0.57 to 283 m/day, and a range in logCa from -7.64 to -4.94 at 40 °C or from -7.46 to -4.76 at 35 °C, respectively. A total of 24 $scCO_2$–water displacement experiments were conducted in this study (Table 1), divided into three independent sets of experiments as follows:

Set I, $DscCO_2$– and $WscCO_2$–water displacement experiments using the M-1 micromodel at 40 °C: $DscCO_2$ was injected into M-1 at a constant flowrate until quasi-steady state was reached (i.e., the saturation of the $scCO_2$ did not change over time). $DscCO_2$–water displacement experiments with four different flow rates ($Q = 10$, 100, 1000, and 5000 uL/h) were conducted. $WscCO_2$ displacement experiments were performed under the same scenario as $DscCO_2$.

Set II, $DscCO_2$– and $WscCO_2$–water displacement experiments using the M-2 micromodel at 40 °C: $DscCO_2$ and $WscCO_2$ were injected into the M-2 micromodel and performed the displacement experiments were performed under the same scenario as Set I, respectively.

Set III, $DscCO_2$– and $WscCO_2$–water displacement experiments using the M-2 micromodel at 35 °C: $DscCO_2$ and $WscCO_2$ were injected into the M-2 micromodel and the displacement experiments were performed under the same scenario as Set II, respectively.

Here, two different supercritical temperatures in Set II and III were conducted to delineate the thermal effects on the behavior of CO_2 migration. A summary of experimental conditions is listed in Table 1. All displacement experiments were conducted horizontally, so density and buoyancy effects were not considered, consistent with approaches in other recent 2D micromodel experiments (Zhang et al. 2011a, b; Wang et al. 2013a; Zuo et al. 2013).

2.4 Image acquisition and analysis

Direct visualization of the $scCO_2$ distribution in the micromodels was obtained using a fluorescent microscope and quantification of saturation in the pore network of micromodel was achieved by image segmentation and pixel counting. Details of the data treatment methods have been described in our previous work (Wang et al. 2013a).

3 Results and discussion

3.1 Water–$scCO_2$ displacement characteristics

Fluorescent images of $scCO_2$ distribution in the micromodel at each injection rate (expressed as logCa) for the three experiment sets are shown in Fig. 1. Each image was obtained after one pore volume (PV) of $scCO_2$ was injected into the pore network, considering at all displacement experiments that (i) CO_2 breaks through the micromodel, (ii) the displacement is at quasi-steady state, and (iii) $scCO_2$ saturation in the micromodel does not significantly change after 1.0 PV of $scCO_2$ injection.

In the $DscCO_2$–water displacement experiments at low injection rates, $DscCO_2$ entered the pore network as a relatively uniform front, followed by randomly distributed forward and lateral migration paths with clusters of entrapped water (Fig. 1, $\log Ca \le -6.64$ for Set I and II, $\log Ca \le -6.46$ for Set III). Approximately halfway through the micromodel, the $DscCO_2$ flow path transitioned into one gradually narrowing finger migrating to the outlet. This displacement mechanism can be classified as capillary fingering dominant. At high injection rate, the $DscCO_2$ entered the pore network at multiple locations in the form of narrow viscous fingers (i.e., 1 ~ 3 pore bodies) (Fig. 1, $\log Ca = -4.94$ for Set I and II, $\log Ca = -4.76$ for Set III). These viscous fingers were distributed across the entire width of the micromodel and mainly progressed forward from the inlet to the outlet. This displacement mechanism can be classified as viscous fingering preferential. At medium injection rate, the $DscCO_2$ front started rather evenly, similar to the formation of capillary fingers, and gradually transitioned to narrower fingers, i.e. viscous fingers (Fig. 1, $\log Ca = -5.64$ at 40 °C, $\log Ca = -5.46$ at 35 °C). These $DscCO_2$ flow paths include a mixture of wide lateral paths and narrow forward progressing paths throughout the entire pore network. This displacement mechanism could be defined as crossover. The same phenomena have been observed by others (Zhang et al. 2011a, b; Wang et al. 2013a).

In the $WscCO_2$–water displacement experiments, at low and medium injection rates, the $WscCO_2$ front started rather evenly and gradually transitioned to one or two narrow fingers (i.e., 1 ~ 3 pore bodies) in a pattern of crossover. At high injection rate, the $WscCO_2$ entered the pore network and displaced water in a pattern of viscous fingering (Fig. 1).

Comparing the $DscCO_2$– with the $WscCO_2$–water displacement experiments, it was observed that at low injection rates, the $scCO_2$ sweep efficiency was much higher in the $DscCO_2$ displacement experiments than that in the $WscCO_2$ displacement experiments. During the stage of capillary fingering, the $DscCO_2$ appears to enhance the lateral and back migration of CO_2 in the micromodel. As a result, the drying effects of $DscCO_2$ combined with the capillary forces are expected to enhance capillary fingering substantially, so that the $DscCO_2$ can positively and forwardly spread and occupy much more pore spaces (Wang et al. 2013a). On the contrary, the dissolved water in $WscCO_2$ appears to limit lateral migration using narrow flow paths, and $WscCO_2$ occupies less pore spaces than $DscCO_2$. At medium and high injection rates, both show similar trends. The crossover and viscous fingering mechanisms were prominent, leading to similar distribution patterns of $DscCO_2$ and $WscCO_2$ displacements. Under condition of 1.0 PV CO_2 injection, $DscCO_2$ might have had limited time of contact with water, affecting the interfacial boundary. Thus, $DscCO_2$ would not impact the stages of crossover and viscous fingering patterns dramatically. The dry-out effects from $DscCO_2$ in such short period or with such small volume injection (1.0 PV) can be ignored due to the small impacts on the displacement processes under the patterns dominated by crossover and viscous fingering.

3.2 $scCO_2$ saturation

The relationship between the S_{scCO2} of the above images (Fig. 1a–c) and the injection rate (logCa) for the above three sets of $DscCO_2$– and $WscCO_2$–water displacement experiments are shown in Fig. 2. The S_{scCO2} of all experiments are listed in Table S2 (SI).

From Fig. 2 and Table S2, in $DscCO_2$–water displacement experiments, S_{scCO2} first increased with increasing logCa during the stage of capillary fingering when the flow pattern was controlled by capillary forces coupled with drying effects from $DscCO_2$ (Fig. 2, upper three curves). Then S_{scCO2} decreased sharply as logCa increased further to the stage of crossover. The decrease is caused by the transition from broad capillary fingers to narrow viscous fingers shortly after $scCO_2$ entered the pore network (Fig. 1). Finally, when viscous fingering dominates the unstable flow at high injection rates, S_{scCO2} increased again as logCa increased. The observation is consistent with previous studies (Zhang et al. 2011a, b; DeHoff et al. 2012; Wang et al. 2013a).

In $WscCO_2$–water displacement experiments, S_{scCO2} increased generally with injection rates (shown in Fig. 2, lower three curves). First, it increased a little when the flow

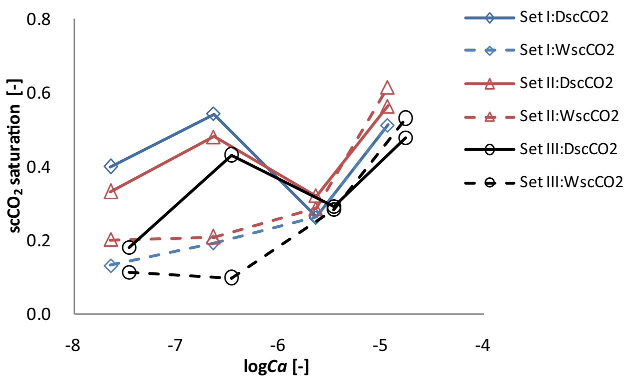

Fig. 2 $scCO_2$ saturation vs. injection rate (logCa) for the three sets of $DscCO_2$– and $WscCO_2$–water displacement experiments

pattern of crossover was observed (i.e., at low and medium logCa) and then was followed by a large increase when viscous fingering was observed (i.e., at high logCa). When the displacement was at viscous fingering dominating pattern, S_{scCO2} can increase by 0.35 ~ 0.47 per logCa. But when the displacement is at a crossover pattern, S_{scCO2} increases 0.04 ~ 0.09 per logCa. It was considered that the dissolved water in $scCO_2$ hindered $scCO_2$ from extracting water any more (i.e., no more drying effects) during the process of $WscCO_2$–water displacement.

We also investigated the influence of the dissolved water in $WscCO_2$ and the drying effects from $DscCO_2$ on S_{scCO2} by comparing the saturation fractions, which were determined by the differential saturation between each pair of $DscCO_2$– and $WscCO_2$–water displacement saturations. The decreased S_{scCO2} fraction due to block of the dissolved water for the three sets of $DscCO_2$– and $WscCO_2$–water displacement experiments are shown in Figure S2(a) (SI). The enhanced S_{scCO2} fraction due to drying effects in all three sets of experiments is shown in Figure S2(b) (SI). The influences of drying-out effect of $DscCO_2$ and dissolved water in $WscCO_2$ are mainly reflected in capillary fingering preferential periods. At the low injection rates, $DscCO_2$ saturation increased up to 4.4 times as compared to that of $WscCO_2$ (Figure S2(a)) and $WscCO_2$ saturation was decreased 0 ~ 0.77 in proportion to that of $DscCO_2$ (Figure S2(b)). However, at medium and high injection rates, S_{scCO2} is approximately the same in $DscCO_2$– and $WscCO_2$–water displacement experiments when crossover and viscous fingering dominate the two-phase flow. Because the dry-out effects from $DscCO_2$ are limited in such short contact duration between CO_2 and water, they make little impact on the displacement processes when the flow patterns are dominated by crossover and viscous fingering.

3.3 Specific interfacial area

The specific interfacial area between $scCO_2$ and water can be approximated by normalizing the surface area of the $scCO_2$ phase obtained from the micromodel images by the total area of the pore network, on the basis that the wetting phase (water) surrounds the solid grains (Zhang et al. 2011a, b). The relations of interfacial area vs. injection rate are shown in Fig. 3. The results of each interfacial area for the three sets of experiments are listed in Table S2 (SI).

From Fig. 3 and Table S2, in $DscCO_2$–water displacement experiments, the specific interfacial area of the $DscCO_2$ displacements first increased slowly when the flow pattern was controlled by capillary forces coupled with drying effects from $DscCO_2$. Then a large decrease in the $DscCO_2$ specific interfacial area was observed in the crossover scenario. When viscous fingering dominated the unstable flow at high injection rates, the $DscCO_2$ specific interfacial area increased again (Fig. 3, upper three curves). In $WscCO_2$–water displacement experiments, the specific interfacial areas were relatively low with a slight fluctuation in the experiments of low and medium injection rates and increased subsequently at high injection rates (Fig. 3, lower three curves).

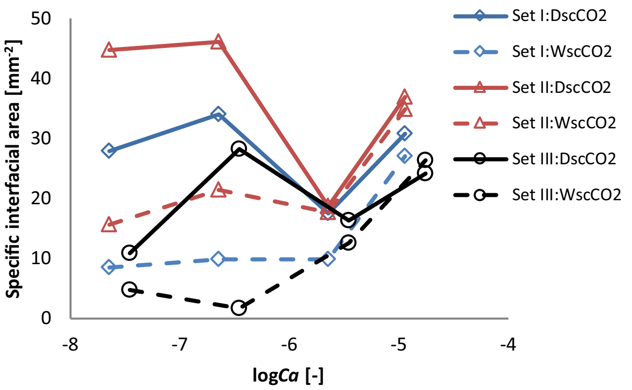

Fig. 3 $scCO_2$ specific interfacial area vs. flow rate (logCa) for the three sets of $DscCO_2$– and $WscCO_2$–water displacement experiments

The influence of the dissolved water in $WscCO_2$ and the drying effects from $DscCO_2$ on the $scCO_2$ specific interfacial area were also investigated by comparing $scCO_2$ specific interfacial area fractions. Those specific interfacial area fractions were determined by the differential specific interfacial area between each pair of $DscCO_2$– and $WscCO_2$–water displacement experiments. The decreased $scCO_2$ specific interfacial area fractions due to the dissolved water for the three sets of $DscCO_2$– and $WscCO_2$–water displacement experiments are shown in Figure S3(a) (SI), and the enlarged $scCO_2$ specific interfacial area fractions due to the drying effects are shown in Figure S3(b) (SI). The maximum WscCO2 specific interfacial area fraction due to the dissolved water was reduced to 0.9. The maximum $DscCO_2$ specific interfacial area fraction due to the drying effects increased up to 16 times compared to that of $WscCO_2$.

Thus, the drying effects of $DscCO_2$ combined with capillary forces play a dominate role in specific interfacial area as well as $scCO_2$ saturation enhancement when capillary fingering dominates the displacement process. Conversely, the dissolved water in $WscCO_2$ adversely influences $WscCO_2$–water displacement, reducing the specific interfacial area and saturation of $WscCO_2$. Thus, the $WscCO_2$ specific interfacial area was lower than that of $DscCO_2$ considerably at lower injection rates. The drying effects from $DscCO_2$ enhanced the specific interfacial area, especially for Set II where the temperature was slightly higher, resulting in a larger dissolved water solubility. In the pattern of crossover from capillary to viscous fingering, a sharp drop in the value of $DscCO_2$ specific interfacial area was observed, indicating the drying effects cannot play an effective role any longer. In addition, From Figs. 2 and 3, the trends of each curve for

CO_2 saturation and the corresponding curve for CO_2 specific interfacial area are almost the same, indicating that the larger the CO_2 specific interfacial area is, the more the CO_2 saturation is, vice versa.

3.4 scCO_2 mobility analysis

Two fractions of the scCO_2 phase in the pore network can be identified from the fluorescent images: a mobile fraction forming active flowpaths through the entire length of the network, and a trapped fraction consisting of clusters of scCO_2 disconnected from the active flowpaths (Wang et al. 2013a). For example, Figure S4 (SI) shows the active flowpaths caused by scCO_2 displacing water in micromodels. Figure 4 shows the volume fractions of mobile scCO_2 at different injection rates. Figure S5(a) and (b) (SI) shows the decreased (due to presence of the dissolved water) and increased (due to the drying effects) scCO_2 volume fraction in active flowpaths across the pore network with the injection rate (log*Ca*) for the three sets of DscCO_2– and WscCO_2–water displacement experiments. The results of volume fraction of mobile scCO_2 for each experiment are listed in Table S2.

From Fig. 4 and Table S2, at low injection rates in DscCO_2–water displacement experiments, where the displacement process was dominated by capillary fingering combined with drying effects from DscCO_2, the mobile fraction accounted for more than 95% of scCO_2 in the pore network, with the remainder trapped as blobs. At high injection rates, where viscous fingering was the dominant displacement mechanism, approximately 89 ~ 98% of scCO_2 was in active flow paths, with the rest as immobile blobs, irrespective to DscCO_2– or WscCO_2–water displacement processes. In the crossover from capillary to viscous fingering, differences between the DscCO_2– or WscCO_2–water displacements were also small. For DscCO_2–water displacements, the mobile fraction was 66.5–80.9%, while values of 19.1–33.5% obtained from the main flow paths as inactive fingers. In the WscCO_2–water displacement experiments, the mobile fraction accounted for 55–89% of scCO_2 in the pore network, with 11–45% as immobile blobs when the displacement process was dominated by crossover. At log*Ca* = − 4.64 (40 °C), almost 89% of scCO_2 was in active flowpaths, which means only 11% was as immobile blobs in the pattern of viscous fingering. From Figure S4 (a) and (b), slight differences in scCO_2 mobile fraction were observed between WscCO_2– and DscCO_2–water displacement processes. The variations of the mobile fractions for experiments Sets I and II under 40 °C were similar, however the trend for experiments Sets II and III at 35 °C differred greatly.

For experiment Set III, scCO_2 mobile fraction accounted for the highest (> 90%) in DscCO_2—water and the lowest (< 25%) in WscCO2–water displacement at low flow rates. The scCO_2 mobile fraction decreased by up to 70% due to the dissolved water in WscCO_2 and increased by as high as 3.7 times due to the dry-out effects from DscCO_2. Large fractions of scCO_2 in active flow paths could potentially influence mutual dissolution between the injected CO_2 phase and trapped water, causing a large initial increase in water acidity and resulting in dry-out of the formation brine. Meanwhile, the drying effects from DscCO_2 further enhanced the scCO_2 volume fraction in active flow paths.

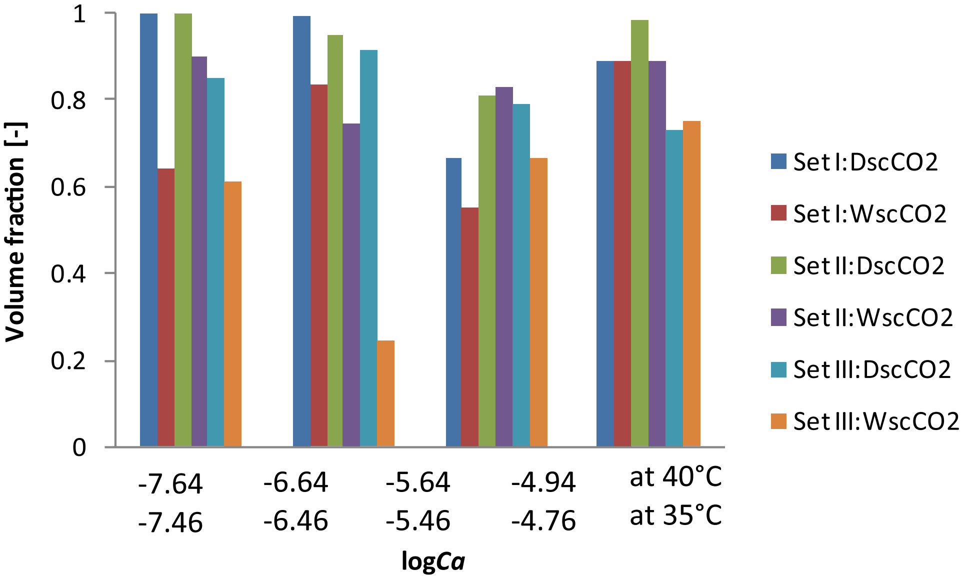

Fig. 4 scCO_2 volume fraction in active flow paths across the pore network *vs.* flow rate for the three sets of DscCO_2– and WscCO_2–water displacement experiments

4 Implications

Due to the unfavorable viscosity ratio (log$M < 0$), unstable displacement of formation brine by $scCO_2$ has been identified as one of the leading causes for the low storage efficiency factor of carbon storage in saline aquifers. Results from the $DscCO_2$–water displacement experiments indicated that, consistent with the results of our previous study (Metz et al. 2005), there are three mechanisms that control $DscCO_2$–water two-phase flow at the pore scale: (i) capillary fingering at low injection rates, (ii) crossover from capillary to viscous fingering at medium injection rates, and (iii) viscous fingering at high injection rates. However, for $WscCO_2$–water displacements, only two mechanisms were observed: (i) crossover at low and medium injection rates, and (ii) viscous fingering at high injection rates. Capillary fingering might occur only at far lower injection rates [e.g., log$Ca < -7.64$ (40 °C)]. With the capillary force combined with the drying effect from $DscCO_2$ affecting the $scCO_2$–water displacement process, larger saturation, specific interfacial areas and mobile of $DscCO_2$ fractions were observed when the capillary fingering dominates the displacement process. The capillary forces combined with drying effects also were identified as one of the leading causes for obtaining a higher $scCO_2$ sweep efficiency.

Results from this study demonstrate the importance of understanding pore-scale displacement mechanisms and the effects of water dissolution on interface of two-phase flow and eventually on sweep efficiency of CO_2. The drying effects from $DscCO_2$ would prompt to extract water from interfacial surface between CO_2 and water, break the interfacial surface and allow CO_2 to penetrate through current pore throat and to the next pore throat as well as to form a new interface whose specific interfacial area, for example, changes from 28.239 to 96.933 cm^{-1} in Set I. Thus, such mutual solubility obviously modifies the radius of wetted perimeter of CO_2 in the micromodel. The specific interfacial length between CO_2 and water doubled and even tripled during the capillary fingering process. In this way, the saturation and sweep efficiency factor of CO_2 have increased dramatically. Furthermore, the dry-out effects of CO_2 can alter capillary boundary or "capillary pressure lock" at the pore throat, enhancing the CO_2 displacement efficiency and CO_2 saturation. One of the reasons why dry-out effect is more efficient in capillary fingering scenario might be that at the scale of micromodel, the slow CO_2 flow is capable of carrying a lot of water moisture out of the micromodel and enhancing the processes of mutual solution and capillary fingering in the micromodel. As a result of variation of water–CO_2 interface at pore scale and difference of CO_2 distribution at microscale caused by dry CO_2, the rock properties measured by laboratory experiments, such as capillary pressure curve and relative permeability, should be used carefully for different state of CO_2. Previous literatures have shown that these properties are dependent on lots of factors, such as flow velocity, geochemistry and flow rate history (Wang et al. 2013b; Loring et al. 2011; Loring et al. 2012; Kazemifar et al. 2016; Roman et al. 2016; Takeshi et al. 2016). Besides, this study implies that the state of CO_2, whatever dry or wet, will certainly affect these properties. Therefore, conventional calibration curves of capillary pressure and relative permeability obtained without consideration of CO_2 state might not adequately describe the complete CO_2–brine displacement process, especially near the wellbore. Thus, proper modifications to the current models are needed to accurately account for the effect of CO_2 saturation enhancement caused by the dry-out effect. For instance, to design an appropriate injection scheme, it will be important to (i) measure the rock properties in both dry or wet $scCO_2$; (ii) utilize dry-out effects in the flow patter of capillary fingering so as to enhance the CO_2 saturation and storage efficiency near the borehole or a certain distance from the borehole; and (iii) build more detailed models considering the dry-out effects and the migration of CO_2.

It should be noted that this study was performed in a nearly homogeneous 2D pore network with well-controlled surface properties. The heterogeneity from the fabrication process likely contributed a little to the complex fingering shape of various migration patterns of CO_2 during the displacement processes. Large variations in pore geometry with different surface wettability, stemming from various lithology and mineralogy, can be expected in geological formations, which will have more pronounced impacts on pore level CO_2 saturation and overall storage capacity.

Acknowledgements All experiments in this research were performed at the William R. Wiley Environmental Molecular Science Laboratory (EMSL), a national scientific user facility sponsored by the US Department of Energy's Office of Biological and Environmental Research and located at the Pacific Northwest National Laboratory, operated for the Department of Energy by Battelle.

Funding This work was supported by the 973 Program of China [Grant number 2014CB239205]; National Natural Science Foundation of China [Grant numbers 41304081]; and Open fund of State Key Laboratory of Oil and Gas Reservoir Geology and Exploitation (Southwest Petroleum University) [Grant numbers PLN201601].

References

Bachu S, Brant B (2008) Effects of in-situ conditions on relative permeability characteristics of CO2 -brine systems. Environ Geol 54:1707–1722. https://doi.org/10.1007/s00254-007-0946-9

Bachu S, Brant Bennion D (2009) Dependence of CO2 -brine interfacial tension on aquifer pressure, temperature and water salinity. Energy Procedia 1:3157–3164

Bennion B, Bachu S (2005) Relative permeability characteristics for supercritical CO_2 Displacing water in a variety of potential sequestration zones in the Western Canada Sedimentary Basin. SPE 95547:1–15. https://doi.org/10.2118/95547-MS

Bennion B, Bachu S (2006a) The impact of interfacial tension and pore-size distribution/capillary pressure character on CO_2 relative permeability at reservoir conditions in CO_2 -brine systems. SPE/DOE symp improv oil recover Tula, Oklahoma, USA, April 22–26. https://doi.org/10.2118/99325-MS

Bennion D, Bachu S (2006b) Dependence on temperature, pressure, and salinity of the IFT and relative permeability displacement characteristics of CO_2 Injected in deep saline aquifers. SPE Annu Tech Conf. https://doi.org/10.2118/102138-MS

Bennion DB, Bachu S (2006c) Supercritical CO_2 and H2S brine drainage and imbibition relative permeability relationships for intergranular sandstone and carbonate formations. SPE Eur Annu Conf Exhib Vienna, Austria, 12–15 June 12–15. https://doi.org/10.2523/99326-MS

Bennion B, Bachu S (2007a) Permeability and relative permeability measurements at reservoir conditions for CO2–water systems in ultra low permeability confining caprocks. Proc Eur Conf Exhib 1–9. https://doi.org/10.2118/106995-MS

Bennion DB, Bachu S (2007b) SPE 106995 permeability and relative permeability measurements at reservoir conditions for CO2 – water systems in ultralow-permeability confining Caprocks. SPE

Bennion B, Bachu S (2008) Drainage and imbibition relative permeability relationships for supercritical CO_2/Brine and H2S/Brine systems in intergranular Sandstone, Carbonate, Shale, and anhydrite rocks. SPE Reserv Eval Eng 11:487–496. https://doi.org/10.2118/99326-PA

Choi YH, Kim J, Noh MJ et al (1998) Effect of functional groups on the solubilities of coumarin derivatives in supercritical carbon dioxide. Chromatographia 47:93–97. https://doi.org/10.1007/BF02466793

Chomsurin C (2003) Analysis of pore-scale nonaqueous phase liquid dissolution in etched silicon pore networks. Water Resour Res 39(9):1265–1275. https://doi.org/10.1029/2002WR001643

Cottin C, Bodiguel H, Colin A (2010) Drainage in two-dimensional porous media: from capillary fingering to viscous flow. Phys Rev E Stat Nonlinear Soft Matter Phys. https://doi.org/10.1103/PhysRevE.82.046315

DeHoff KJ, Oostrom M, Zhang C, Grate JW (2012) Evaluation of two-phase relative permeability and capillary pressure relations for unstable displacements in a pore network. Vadose Zo J. https://doi.org/10.2136/vzj2012.0024

Ferer M, Ji C, Bromhal GS et al (2004) Crossover from capillary fingering to viscous fingering for immiscible unstable flow: Experiment and modeling. Phys Rev E Stat Nonlinear Soft Matter Phys. https://doi.org/10.1103/PhysRevE.70.016303

Hatiboglu CU, Babadagli T (2010) Experimental and visual analysis of co- and counter-current spontaneous imbibition for different viscosity ratios, interfacial tensions, and wettabilities. J Pet Sci Eng 70:214–228. https://doi.org/10.1016/j.petrol.2009.11.013

Kazemifar F, Blois G, Kyritsis CD, Christensen TK (2016) Quantifying the flow dynamics of supercritical CO2–water displacement in a 2D porous micromodel using fluorescent microscopy and microscopic PIV. Adv Water Resour 95:352–368

Lengler U, De Lucia M, Kühn M (2010) The impact of heterogeneity on the distribution of CO2: numerical simulation of CO_2 storage at Ketzin. Int J Greenh Gas Control 4:1016–1025. https://doi.org/10.1016/j.ijggc.2010.07.004

Lenormand R, Touboul E, Zarcone C (1988) Numerical models and experiments on immiscible displacements in porous media. J Fluid Mech 189:165. https://doi.org/10.1017/S0022112088000953

Lopez O, Idowu N, Mock A et al (2011) Pore-scale modelling of CO2-brine flow properties at In Salah, Algeria. Energy Procedia 4:3762–3769. https://doi.org/10.1016/j.egypro.2011.02.310

Loring JS, Wang Z, Thompson CJ et al (2010) Carbonation of forsterite exposed to water-saturated supercritical carbon dioxide. Geochim Cosmochim Acta 74:A631–A631

Loring JS, Thompson CJ, Wang Z et al (2011) In situ infrared spectroscopic study of forsterite carbonation in wet supercritical CO_2. Environ Sci Technol 45:6204–6210. https://doi.org/10.1021/es201284e

Loring JS, Thompson CJ, Zhang C et al (2012) In situ infrared spectroscopic study of brucite carbonation in dry to water-saturated supercritical carbon dioxide. J Phys Chem A 116:4768–4777. https://doi.org/10.1021/jp210020t

Lu C, Han WS, Lee SY et al (2009) Effects of density and mutual solubility of a CO_2-brine system on CO2 storage in geological formations: "Warm" vs. "cold" formations. Adv Water Resour 32:1685–1702. https://doi.org/10.1016/j.advwatres.2009.07.008

Mahadevan J, Sharma MM, Yortsos YC (2007) Water removal from porous media by gas injection: experiments and simulation. Transp Porous Media 66:287–309. https://doi.org/10.1007/s11242-006-0030-z

McCaughan J, Iglauer S, Bresme F (2013) Molecular dynamics simulation of water/CO_2-quartz interfacial properties: Application to subsurface gas injection. Energy Procedia 37:5387–5402. https://doi.org/10.1016/j.egypro.2013.06.457

Metz B, Davidson O, de Coninck H et al (2005) IPCC Special Report on Carbon Dioxide Capture and Storage

Mohammadi S, Hossein Ghazanfari M, Masihi M (2013) A pore-level screening study on miscible/immiscible displacements in heterogeneous models. J Pet Sci Eng 110:40–54. https://doi.org/10.1016/j.petrol.2013.08.043

Nordbotten JM, Celia MA, Bachu S (2005) Injection and storage of CO2 in deep saline aquifers: analytical solution for CO2 plume evolution during injection. Transp Porous Media 58:339–360. https://doi.org/10.1007/s11242-004-0670-9

Pruess K (2009) Formation dry-out from CO2 injection into saline aquifers: 2. analytical model for salt precipitation. Water Resour Res. https://doi.org/10.1029/2008WR007102

Pruess K, Müller N (2009) Formation dry-out from CO2 injection into saline aquifers: 1. effects of solids precipitation and their mitigation. Water Resour Res. https://doi.org/10.1029/2008WR007101

Roman S, Soulaine C, AlSaud MA et al (2016) Paricle velocimetry analysis of immiscible two-phase flow in micromodels. Adv Water Resour 95:199–211

Sohrabi M, Kechut NI, Riazi M et al (2011) Safe storage of CO2 together with improved oil recovery by CO_2-enriched water injection. Chem Eng Res Des 89:1865–1872. https://doi.org/10.1016/j.cherd.2011.01.027

Spycher N, Pruess K, Ennis-King J (2003) CO_2-H_2O mixtures in the geological sequestration of CO_2. I. Assessment and calculation of mutual solubilities from 12 to 100 °C and up to 600 bar. Geochim Cosmochim Acta 67:3015–3031. https://doi.org/10.1016/S0016-7037(03)00273-4

Takeshi T, Fei J, Kenneth TC (2016) Characterization of immiscible fluid displacement processes with various capillary numbers and viscosity ratios in 3D natural sandstone. Adv Water Resour 95:3–15

Wang Y, Zhang C, Wei N et al (2013a) Experimental study of crossover from capillary to viscous fingering for supercritical CO_2–water displacement in a homogeneous pore network. Environ Sci Technol 47:212–218. https://doi.org/10.1021/es3014503

Wang Z, Felmy AR, Thompson CJ et al (2013b) Near-infrared spectroscopic investigation of water in supercritical CO2 and the effect of CaCl2. Fluid Phase Equilib 338:155–163. https://doi.org/10.1016/j.fluid.2012.11.012

Willingham TW, Werth CJ, Valocchi AJ (2008) Evaluation of the effects of porous media structure on mixing-controlled reactions using pore-scale modeling and micromodel experiments. Environ Sci Technol 42:3185–3193. https://doi.org/10.1021/es7022835

Xu T, Apps JA, Pruess K (2005) Mineral sequestration of carbon dioxide in a sandstone-shale system. Chem Geol 217:295–318

Zhang C, Oostrom M, Grate JW et al (2011a) Liquid CO2 displacement of water in a dual-permeability pore network micromodel. Environ Sci Technol 45:7581–7588. https://doi.org/10.1021/es201858r

Zhang C, Oostrom M, Wietsma TW et al (2011b) Influence of viscous and capillary forces on immiscible fluid displacement: Pore-scale experimental study in a water-wet micromodel demonstrating viscous and capillary fingering. Energy Fuels 25:3493–3505. https://doi.org/10.1021/ef101732k

Zhao Y, Song Y, Liu Y et al (2011) Visualization of CO2 and oil immiscible and miscible flow processes in porous media using NMR micro-imaging. Pet Sci 8:183–193. https://doi.org/10.1007/s12182-011-0133-1

Zhou Q, Birkholzer JT, Mehnert E et al (2010) Modeling basin- and plume-scale processes of CO_2 storage for full-scale deployment. Ground Water 48:494–514. https://doi.org/10.1111/j.1745-6584.2009.00657.x

Zuo L, Zhang C, Falta RW, Benson SM (2013) Micromodel investigations of CO2 exsolution from carbonated water in sedimentary rocks. Adv Water Resour 53:188–197. https://doi.org/10.1016/j.advwatres.2012.11.004